Springer

KSME

Journal of Mechanical Science and Technology 33 (9) (2019) 4093~4104
www.springerlink.com/content/1738-494x(Print)/1976-3824(Online)
DOI 10.1007/s12206-019-0804-1

Energy-efficient wing design for flapping wing micro aerial vehicles †

Zhonglai Wang[1,2,*], Xiaorong Hu[1,2] and Yingdong Wu[1,2]

[1]*School of Mechanical and Electrical Engineering, University of Electronic Science and Technology of China, Chengdu 611731, China*
[2]*Center for System Reliability and Safety, University of Electronic Science and Technology of China, Chengdu 611731, China*

(Manuscript Received January 9, 2019; Revised May 17, 2019; Accepted May 24, 2019)

Abstract

Flapping wing micro aerial vehicles (FWMAVs) have attracted more attention during the development of the robotic systems field. The size of the flapping wing plays an important role in the lift force and torque generation based on quasi-steady aerodynamic model. Therefore, it is necessary to study energy-efficient design methods for wings to provide sufficient lift force and torque with minimal energy consumption for hovering flight. In this paper, the sensitive parameters for the lift force and power consumption were first selected based on design of experiment (DOE) and the parameter of the distributed wing stiffness was determined based on experimental data. Design optimization models for three different cases were then built by considering the lift force as one constraint and the energy consumption as the objective function. The combination of subset simulation and the gradient-based optimization was finally used for solving design optimization models, and the corresponding sensitivity analysis was provided.

Keywords: Design optimization; Aerodynamic model; Energy-efficient; Hovering flight; Parameter determination; Sensitivity analysis

1. Introduction

Because of the advantages of small size, high agility, and the ability to hover in the air, FWMAVs have attracted more attention from academic and industrial fields. The flapping wing is an important part of the FWMAVs to produce lift force. Therefore, studying the morphology and kinematics of wings and then designing the corresponding energy-saving wings are new focuses.

There have been many studies on the properties of morphology, kinematics and aerodynamics for wings. Rayner proposed a theory on vorticity presented in the wake of hovering animal and estimated the rate of working [1]. Ellington et al. studied the aerodynamics of hovering insect flights, e.g.: Quasi-steady analysis, and morphological parameters [2-4]. Wang et al. studied the wing morphology, flapping kinematics and further proposed a quasi-steady aerodynamic model [5, 6]. Wang et al. also studied the design optimization of wings based on Beta probability density function (BPDF) [6-8]. For energy-effective hovering and roll control, Peters focused on a combined approach to finding an optimal wing design, including wing planform and pitching kinematics [9, 10]. Nan et al. conducted studies on the effect of the wing geometry on the performance including the lift force and energy consumption via experiments [11]. Sane provided a review on the high lift mechanism about insect flight [12]. Stewart et al. used a modified Zimmerman method to investigate the aerodynamic performance of flapping wings [13]. Ghommem et al. established the geometric model of the wing through B-spline representation and optimized the flapping wing shape [14]. For hummingbirds or hummingbird-like MAVs, there are some new developments. Warrick et al. tested and analyzed the differences in aerodynamic mechanisms of the hovering hummingbird between upstroke and downstroke using digital particle imaging velocimetry (DPIV) [15]. Keennon et al. provided state of the art of the development and design of the nano hummingbird [16]. Karásek et al. presented a newfangled flapping mechanism in a robotic hummingbird for the pitch moment generation [17].

A series of studies on the energy requirements of insects or FWMAVs have been carried out. Sun and Du studied energy requirements of eight species of insects including fruit fly, hawkmoth, etc. [18]. The study showed that the major part of energy consumption came from aerodynamic force or wing inertia associated with insect size and wingbeat frequency. Insects can use their muscles and elastic elements to recycle the energy for efficient flight, and change the flight attitude or flapping frequency to adapt to different flight states [19-21]. For the hovering insect flight, Berman et al. investigated efficient energy kinematics and conducted sensitivity analysis for the optimal solutions [22]. For the flight of MAVs, Woods et al. [23] provided energy requirements for the fixed wing mode, rotary wing mode and flapping wing mode, respectively. Ma-

*Corresponding author. Tel.: +86 15881043536, Fax.: +86 2861830227
E-mail address: wzhonglai@uestc.edu.cn
† Recommended by Associate Editor Sungsoo Na
© KSME & Springer 2019

dangopal et al. [24] designed an energy storage mechanism and simplified the wing model by imitating insects, which could store part of the kinetic energy as potential energy similar to an insect thorax.

To further improve the energy efficiency of the hover flight under the satisfaction of constraints, we conducted design optimization of the wing of FWMAVs. The contribution of the paper can be summarized as: (1) The DOE is employed for sensitive parameter selection by considering lift force and energy consumption; (2) a method is provided to determine the distributed wing stiffness using experimental data; (3) design optimization models considering quasi-steady aerodynamic and power consumption model for three cases are built, respectively; (4) the combination of subset simulation and gradient-based optimization is used for solving the three design optimization models.

The paper is organized as follows. In Sec. 2, the quasi-steady aerodynamic model is briefly introduced. Sec. 3 gives the DOE method for sensitive parameters selection by considering lift force and energy consumption. The distributed wing stiffness determination method based on experimental data is provided in Sec. 4. Sec. 5 elaborates on the details of design optimization and sensitivity analysis for the three cases. Conclusions are made in Sec. 6.

2. Quasi-steady aerodynamic and power consumption model

To understand clearly the DOE, parameter determination and design optimization in the next sections, the geometric and kinematic parameters of the wing, aerodynamic model, and energy consumption model are reviewed in this section.

2.1 Geometric parameters of the wing

The shape of the wing where the experiments are conducted is given in Fig. 1 [11]. For simplicity, we modify it as a right angle trapezoid and the diagram is shown in Fig. 2, where we can see the morphological parameters, wing span (R), wing root chord (C_R) and wing tip chord (C_T). However the modification will impose little effect on the lift force and energy consumption. The aspect ratio (AR) is an important parameter, which is usually defined as the ratio of the wing span (R) to the mean chord length ($\bar{c}$). The wing area (S) can be then expressed as

$$S = R\bar{c} = \frac{R^2}{AR} . \tag{1}$$

The chord length can be expressed as a function of the spanwise radius r

$$c = C_R - \frac{C_R - C_T}{R} \times r = C_R - \left(2C_R - \frac{2R}{AR}\right) \times \frac{r}{R} . \tag{2}$$

To describe the spanwise area distribution, the normalized parameter $\hat{d}$ expressing the chord-normalized distance from the pitching axis to the leading edge is introduced. Obviously, when the straight leading edge is considered as the pitching axis in our prototype, the parameter $\hat{d}$ representing the position of the pitching axis will be set to 0.

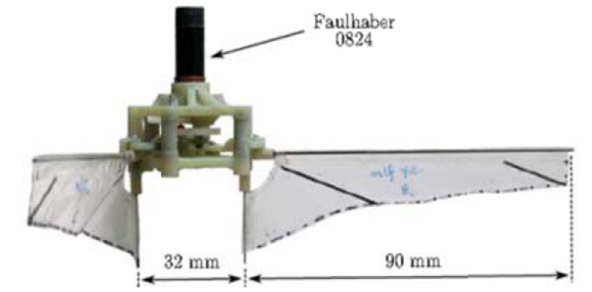

Fig. 1. The geometric shape of the wing [11].

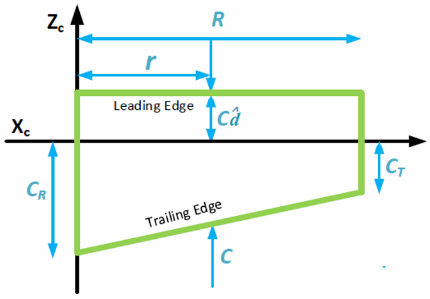

Fig. 2. The modified geometric shape of the wing.

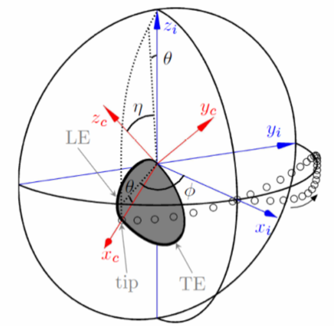

Fig. 3. Definition of angles [6].

2.2 Kinematic parameters of the wing

The reciprocating motion of the wing can be generally divided into three progressive movements: sweeping motion, heaving motion, and pitching motion. Three Euler angles, including the sweeping angle ϕ , heaving angle θ and pitching angle η , are introduced to express these three motions. Two coordinate systems, inertial frame $x_i y_i z_i$ and corotating frame $x_c y_c z_c$, are used to define these angles, shown in Fig. 3 [6]. With the defined framework in Fig. 3, the axis is corresponding to the pitching axis and the axis is parallel to the plane with the wing in Fig. 2.

For hovering flight, the sweeping motion can be described as

$$\phi(t) = \frac{\phi_m}{\arcsin K}\arcsin\left[K\sin(2\pi ft)\right] + \phi_0 \tag{3}$$

where ϕ_m, ϕ_0 and f denote the sweeping amplitude, horizontal offset and frequency, respectively. K is a coefficient to determine the motion pattern and $0 < K < 1$. If $K \to 1$, the motion will be a triangular pattern; if $K \to 0$, the motion will be sinusoidal. According to the motion requirements, we consider the sweeping motion to be approximately sinusoidal and set $K = 0.01$ in our paper.

The heaving motion is described by a sinusoidal function,

$$\theta(\mathrm{t}) = \theta_m \sin(2\pi Nft + \Phi_\theta) + \theta_0 \tag{4}$$

where θ_m, Φ_θ and θ_0 are heaving amplitude, heaving phase offset and heaving offset, respectively. N is selected as 1 or 2. When $N = 1$, the shape of the wing motion will be vertical oscillation, and $N = 2$ corresponds to a figure "8" [22].

For the pitching motion, there is a relationship between the pitching angle and geometric angle of attack (AOA) on condition that the heaving motion is ignored [6], $\alpha_{geo} = 90^\circ - |\eta|$. According to Euler's second law, an implicit function of the pitching angle can be derived as [5, 6]

$$\begin{aligned}
I_{x_c x_c}\ddot{\eta} = {} & \frac{1}{2}I_{x_c x_c}\left[\dot{\phi}^2\cos^2\theta\sin(2\eta) - \dot{\theta}^2\sin(2\eta)\right] \\
& + I_{x_c x_c}\left[2\dot{\phi}\dot{\theta}\cos\theta\cos^2\eta + \ddot{\phi}\sin\theta\right] \\
& + I_{x_c z_c}\left[\ddot{\theta}\sin\eta + \frac{1}{2}\dot{\phi}^2\sin(2\theta)\sin\eta\right] \\
& + I_{x_c z_c}\left[2\dot{\phi}\dot{\theta}\sin\theta\cos\eta - \ddot{\phi}\cos\theta\cos\eta\right] \\
& + \tau_{x_c}^{\mathrm{aero}} - k_\eta \eta
\end{aligned} \tag{5}$$

where $I_{x_c x_c}$ and $\tau_{x_c}^{\mathrm{aero}}$ are $x_c x_c$ terms of the moment of inertia I and aerodynamic torque, respectively. In Nan's experiment, different elastic performance is exhibited due to different wing shape and the angle of stiffener but no quantitative relationship is provided [11]. While in Wang's wing model, a linear torsional spring linked to the wing root is used to represent the flexibility of the wing model [6, 8]. In this paper, we used a parameter k_η to express the distributed wing stiffness. Due to the lack of knowledge about the distribution of the wing mass, we also assumed that the distributed wing mass is uniformly as that in Ref. [6].

Using the "cans in series" approach for coordinate transformations [25], the angular velocity $\boldsymbol{\omega}_\mathbf{c}$ and acceleration can be derived

$$\boldsymbol{\omega}_\mathbf{c} = \begin{bmatrix} \dot{\eta} - \dot{\phi}\sin\theta \\ \dot{\theta}\cos\eta + \dot{\phi}\cos\theta\sin\eta \\ \dot{\phi}\cos\eta\cos\theta - \dot{\theta}\sin\eta \end{bmatrix}, \tag{6}$$

$$\boldsymbol{\alpha}_\mathbf{c} = \left[\alpha_{x_c}, \alpha_{y_c}, \alpha_{z_c}\right]^T = \left[\dot{\omega}_{x_c}, \dot{\omega}_{y_c}, \dot{\omega}_{z_c}\right]^T. \tag{7}$$

From the point of the wing with co-rotating coordinate $\mathbf{r} = (x_c \quad 0 \quad z_c)^{\mathrm{T}}$, the translational velocity and acceleration can be calculated by

$$v_c = \omega_c \times r\ , \tag{8}$$

$$a_c = \alpha_c \times r + \omega_c \times v_c\ . \tag{9}$$

2.3 Aerodynamic model

The aerodynamic model in Ref. [5] is employed here and the resultant aerodynamic load is decomposed into translation-induced load, rotation-induced load, coupling load between wing translation and rotation, and added-mass load. The wing plane is discretized into infinitesimal strips along the chordwise and spanwise directions with the use of the blade element method (BEM) [26]. Since the leading edge of the flapping wing is considered as the pitching axis, the parameter $\hat{d}$ representing the position of the pitching axis is set to 0.

The translation-induced load including force and torque can be expressed as

$$F_{y_c}^{\mathrm{trans}} = A^{\mathrm{trans}}\int_0^R x_c^2 c\,dx_c\ , \tag{10a}$$

$$\tau_{x_c}^{\mathrm{trans}} = \begin{cases} A^{\mathrm{trans}}(\hat{z}_{cp}^{\mathrm{trans}} - \hat{d})\int_0^R x_c^2 c^2 dx_c, & \omega_{y_c} \le 0 \\ A^{\mathrm{trans}}\left(1 - \hat{z}_{cp}^{\mathrm{trans}} - \hat{d}\right)\int_0^R x_c^2 c^2 dx_c, & \omega_{y_c} > 0, \end{cases} \tag{10b}$$

$$\tau_{z_c}^{\mathrm{trans}} = A^{\mathrm{trans}}\int_0^R x_c^3 c\,dx_c\ , \tag{10c}$$

$$A^{\mathrm{trans}} = -\frac{1}{2}\mathrm{sgn}\left(\omega_{z_c}\right)\rho_{\mathrm{f}}\left(\omega_{y_c}^2 + \omega_{z_c}^2\right)C_{F_{y_c}}^{\mathrm{trans}} \tag{10d}$$

where $\mathrm{sgn}(\bullet)$, ρ_{f}, $C_{F_{y_c}}^{\mathrm{trans}}$ and $\hat{z}_{cp}^{\mathrm{trans}}$ are the sign function, fluid density, translational force coefficient and normalized chordwise center of pressure, respectively. The translational force coefficient can be expressed as a function of the angle of attack $\hat{\alpha}$ and aspect ratio

$$C_{F_{y_c}}^{\mathrm{trans}} = \frac{2\pi AR\sin(\hat{\alpha})}{2 + \sqrt{AR^2 + 4}}\ . \tag{11}$$

$\hat{z}_{cp}^{\mathrm{trans}}$ has the special relationship with the angle of attack based on experimental data as

$$\hat{z}_{cp}^{\mathrm{trans}} = 5.6 \times 10^{-3}\hat{\alpha}\ . \tag{12}$$

The rotation-induced load can be expressed as

$$F_{y_c}^{\mathrm{rot}} = \frac{1}{2}\rho_{\mathrm{f}}\omega_{x_c}\left|\omega_{x_c}\right|C_D^{\mathrm{rot}}\int_0^R\int_{\hat{d}c-c}^{\hat{d}c} z_c|z_c|\,dz_c dx_c\ , \tag{13a}$$

$$\tau_{x_c}^{\mathrm{rot}} = -\frac{1}{2}\rho_{\mathrm{f}}\omega_{x_c}\left|\omega_{x_c}\right|C_D^{\mathrm{rot}}\int_0^R\int_{\hat{d}c-c}^{\hat{d}c} |z_c|^3\,dz_c dx_c\ , \tag{13b}$$

$$\tau_{z_c}^{\text{rot}} = \frac{1}{2}\rho_f \omega_{x_c} \left|\omega_{x_c}\right| C_D^{\text{rot}} \int_0^R \int_{\hat{d}c-c}^{\hat{d}c} z_c \left|z_c\right| x_c dz_c dx_c \tag{13c}$$

where C_D^{rot} indicates the rotational damping coefficient, which can be expressed as

$$C_D^{\text{rot}} = \frac{2\pi AR}{2+\sqrt{AR^2+4}} . \tag{14}$$

The coupling load between the wing translation and rotation can be calculated as

$$F_{y_c}^{\text{coup}} = \begin{cases} A^{\text{coup}} \int_0^R \left(1-\hat{d}\right) c^2 x_c dx_c , & \omega_{y_c} \le 0 \\ A^{\text{coup}} \int_0^R \hat{d} c^2 x_c dx_c , & \omega_{y_c} > 0 , \end{cases} \tag{15a}$$

$$\tau_{x_c}^{\text{coup}} = \begin{cases} A^{\text{coup}} \int_0^R \left(\frac{3}{4}-\hat{d}\right)\left(\frac{1}{2}-\hat{d}\right) c^3 x_c dx_c , \omega_{y_c} \le 0 \\ A^{\text{coup}} \int_0^R \left(\hat{d}-\frac{1}{4}\right)\left(\frac{1}{2}-\hat{d}\right) c^3 x_c dx_c , \ \omega_{y_c} > 0 , \end{cases} \tag{15b}$$

$$\tau_{z_c}^{\text{coup}} = \begin{cases} A^{\text{coup}} \int_0^R \left(1-\hat{d}\right) c^2 \left(x_c\right) x_c^2 dx_c , & \omega_{y_c} \le 0 \\ A^{\text{coup}} \int_0^R \hat{d} c^2 \left(x_c\right) x_c^2 dx_c , & \omega_{y_c} > 0 , \end{cases} \tag{15c}$$

$$A^{\text{coup}} = \pi\rho\omega_{x_c}\omega_{y_c} . \tag{15d}$$

The added-mass loads are given by

$$F_{y_c}^{\text{am}} = -\int_0^R m_{22} a_{y_c} dx_c - \alpha_{x_c} \int_0^R m_{24} dx_c , \tag{16a}$$

$$\tau_{x_c}^{\text{am}} = -\int_0^R m_{42} a_{y_c} dx_c - \alpha_{x_c} \int_0^R m_{44} dx_c , \tag{16b}$$

$$\tau_{z_c}^{\text{am}} = -\int_0^R m_{22} a_{y_c} x_c dx_c - \alpha_{x_c} \int_0^R m_{24} x_c dx_c , \tag{16c}$$

$$\begin{bmatrix} m_{22} & m_{24} \\ m_{42} & m_{44} \end{bmatrix} = \frac{\pi}{4}\rho \begin{bmatrix} c^2 & c^3\left(1/2-\hat{d}\right) \\ c^3\left(1/2-\hat{d}\right) & c^4/32 + c^4\left(1/2-\hat{d}\right)^2 \end{bmatrix} . \tag{16d}$$

Due to the assumption that the resultant force is perpendicular to the wing during the entire stroke, the force about x_c and z_c axis and the torque about y_c axis are zero. Then the resultant loads can be written as

$$F_{y_c}^{\text{aero}} = F_{y_c}^{\text{trans}} + F_{y_c}^{\text{rot}} + F_{y_c}^{\text{coup}} + F_{y_c}^{\text{am}} , \tag{17a}$$

$$\tau_{x_c}^{\text{aero}} = \tau_{x_c}^{\text{trans}} + \tau_{x_c}^{\text{rot}} + \tau_{x_c}^{\text{coup}} + \tau_{x_c}^{\text{am}} , \tag{17b}$$

$$\tau_{z_c}^{\text{aero}} = \tau_{z_c}^{\text{trans}} + \tau_{z_c}^{\text{rot}} + \tau_{z_c}^{\text{coup}} + \tau_{z_c}^{\text{am}} . \tag{17c}$$

2.4 Energy consumption model

Considering the flexible structure of the wing, there are three parts in the energy consumption model: the energy to overcome the aerodynamic drag (P_{aero}), the energy to accelerate the wing and the surrounding medium (P_{iner}), and the energy stored in the elastic structure (P_{elas}) [27]. They are expressed as

$$P_{\text{aero}} = -\tau_{x_c}^{\text{aero}}\omega_{x_c} - \tau_{z_c}^{\text{aero}}\omega_{z_c} , \tag{18a}$$

$$P_{\text{iner}} = -\tau_{x_c}^{\text{iner}}\omega_{x_c} - \tau_{y_c}^{\text{iner}}\omega_{y_c} - \tau_{z_c}^{\text{iner}}\omega_{z_c} , \tag{18b}$$

$$P_{\text{elas}} = k_\eta \eta \omega_{x_c} . \tag{18c}$$

The inertial torque $\boldsymbol{\tau}^{\text{iner}}$ can be calculated in the co-rotating frame as

$$\tau^{iner} = -I\alpha_c - \omega_c \times \left(I\omega_c\right) . \tag{19}$$

Since the kinetic energy and elastic energy are either used to compensate the power consumed by the drag or recycled by the drive mechanism, the actual flapping power consumption can be estimated in two extreme cases. The maximum and minimum energy consumption can be calculated as

$$P_{\text{min}} = \frac{1}{T}\int_T P_{\text{aero}} dt , \tag{20a}$$

$$P_{\text{max}} = \frac{1}{T}\int_T \Xi\left(P_{\text{aero}} + P_{\text{iner}} + P_{\text{elas}}\right) dt . \tag{20b}$$

The actual energy consumption is between P_{min} and P_{max}. For the optimization, the maximum consumption is our focus; therefore, the total mass-normalized power consumption P^* is accounted for

$$P^* = \frac{\frac{1}{T}\int_T \Xi\left(P_{\text{aero}} + P_{\text{iner}} + P_{\text{elas}}\right) dt}{total\ mass} \tag{21}$$

where Ξ is a sign, when $P_{\text{aero}} + P_{\text{iner}} + P_{\text{elas}} \le 0$, $\Xi = 0$, else $\Xi = P_{\text{aero}} + P_{\text{iner}} + P_{\text{elas}}$. T represents a stroke cycle of the flapping flight including upstroke and downstroke. For more details, please refer to Refs. [5, 6, 8, 27].

3. Sensitive parameters selection for design optimization

It is necessary to select sensitive parameters for building design optimization models to reduce the computational expense. Therefore we use 3-level fractional factorial DOE approach to qualitatively selecting several sensitive parameters. The main effect analysis for the lift force to each variable is conducted and the main effects are shown in Fig. 4.

The order of the variables from the aspect of sensitivity to the lift force is $AR > \phi_m > C_R > R > f > k_\eta$. The same procedure is used for energy consumption, the main effects are shown in Fig. 5. From Fig. 5, we know that the order of the variables from the aspect of sensitivity to the energy consumption is $\phi_m > AR > R > f > k_\eta > C_R$, which is roughly similar to that of the lift force. Since the main effect of C_R is not obvious for energy consumption, and $C_R = 25$ mm based on experimental results. Therefore R, ϕ_m, f, k_η and AR are considered as design variables for design optimization.

Table 1. The lift at different frequency level.

	Lift (mN)		
AR	$f=10$ Hz	$f=20$ Hz	$f=22$ Hz
2.8	4.50	62.82	76.44
3.2	9.34	72.27	86.82
3.65	17.29	74.78	91.66
4.13	23.17	80.91	98.92
4.63	24.21	100.51	120.71
5.14	24.90	106.34	128.32
5.7	23.87	111.57	134.55

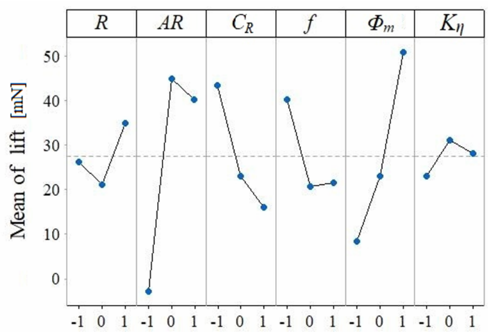

Fig. 4. Tree-level main effects for lift force.

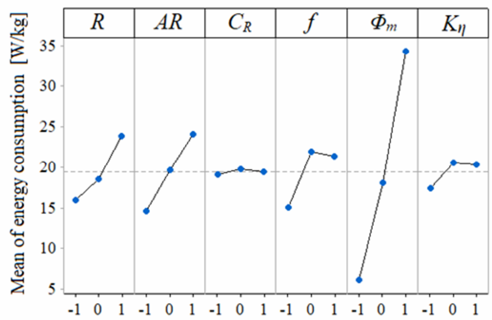

Fig. 5. Tree-level main effects for normalized energy consumption.

4. Determination of the distributed wing stiffness based on experimental data

The distributed wing stiffness k_η is a morphological parameter that affects the lift force and also energy consumption. The parameter should be first determined for the design optimization for morphological parameters. However, it could not be measured via experiments. In this section, the parameters are determined based on the experimental data using the least square method, shown in Table 1 [11].

The corresponding optimization model is built under the provided parameters $\left[C_R \quad f \quad \phi_m \quad S\right]=\left[25 \quad 10 \quad 90° \quad 1750\right]$,

$$\begin{cases} Find & k_\eta \\ \min & |L|^2=\sum_{i=1}^{7}\left|Lift_{\text{theor}}(i)-Lift_{\text{exper}}(i)\right|^2 \\ s.t. & 0\le k_\eta \le 15\times 10^{-4}\,. \end{cases} \tag{22}$$

Table 2. The relationship between R, S and lift at different frequency level.

		Lift (mN)			
R (mm)	*S* (mm^2)	$f=14$ Hz	$f=16$ Hz	$f=18$ Hz	$f=22$ Hz
70	1059	15.80	21.32	28.09	43.77
75	1215	21.90	28.24	36.70	57.20
80	1383	29.52	40.24	52.05	78.52
85	1561	39.66	50.16	65.77	97.35
90	1750	48.42	64.10	80.58	121.08
95	1950	56.72	77.24	99.09	144.82
100	2161	69.29	90.04	111.61	155.71

The optimization is carried out via a gradient-based optimization method and the result is $k_\eta=9.6\times10^{-4}$.

To verify whether the determined parameter fits the experimental data well or not, graphical results for the model analysis are given in Fig. 6. From Fig. 6, we know that the theoretical values approximately fit the experimental values. The errors are from the theoretical model and also uncertainty from experiments [28, 29]. To further verify the effectiveness of the determined parameter, other experiments data for different area are employed, shown in Table 2 [11]. The corresponding graphical results for the model analysis are given in Fig. 7.

From Figs. 6 and 7, we can conclude that the determined parameter $k_\eta=9.6\times10^{-4}$ and also the lift force model is approximately suitable to describe the physical prototype. Therefore, it is proper to use the parameter and model to conduct sequential design optimization.

5. Design optimization and sensitivity analysis

In this section, three design optimization models will be elaborated considering the morphological parameters, and both morphological and kinematic parameters respectively for the trapezoidal wings of the hummingbird-like MAV. Design optimization and sensitivity analysis are conducted for the hovering status here. The combination of subset simulation and gradient-based optimization will be implemented for solving the three design optimization models. Subset simulation is generally robust to deal with high-dimensional constrained optimization problems [30-32]. There are two steps for the combined optimization algorithm: (1) Subset simulation optimization with *N* generated independent samples is employed for locating the initial point near the global optimal point for the gradient-based optimization and *N* is usually set to be several hundreds; (2) gradient-based optimization is conducted with the optimal point provided by subset simulation as the initial point for reducing the probability of sinking into local optimal points.

During the design optimization for morphological parameters, only the geometric parameters and flapping frequency are considered as design variables, e.g.: R, AR and f. While

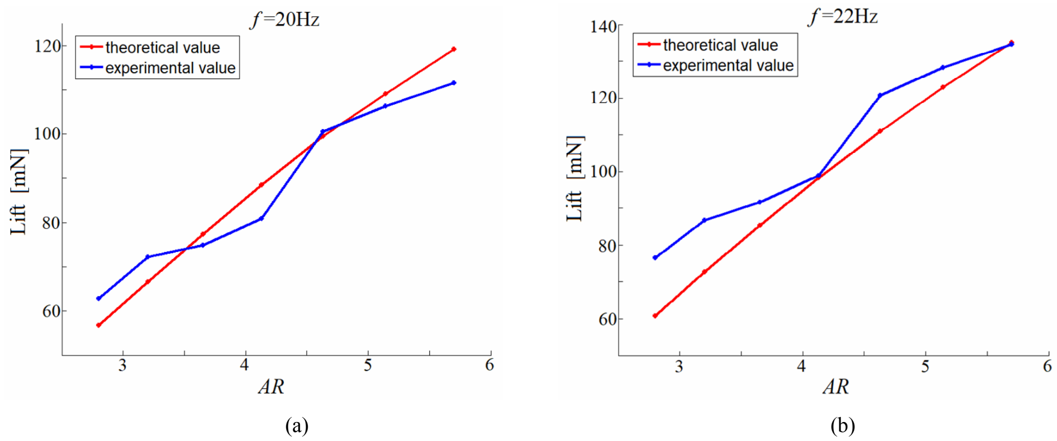

Fig. 6. Comparison between theoretical and experimental results for the same area.

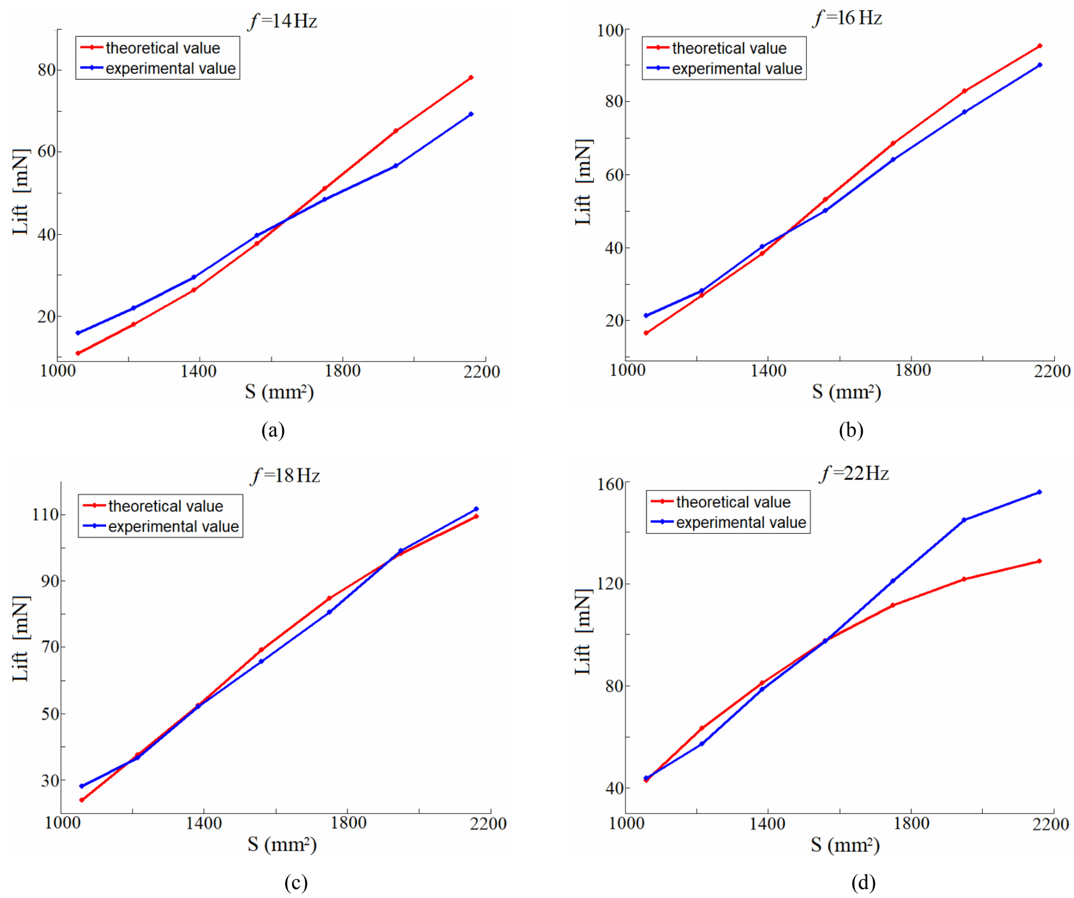

Fig. 7. Comparison between theoretical and experimental results for different area.

during the design optimization for both morphological and kinematic parameters, the morphological and kinematic parameters, i.e.: R, AR, f, ϕ_m and k_η, are considered as design variables. The objective is to minimize the energy consumption, while the constraints are the lift force and other performance and geometric parameters. The constraint boundaries for design variables are derived from experiments and theoretical analysis, shown in Table 3. For searching the possible optimal results, we expand properly the design domain for the design optimization for morphological and kinematic parameters.

5.1 Design optimization for morphological parameters

Design optimization model for morphological parameters is given by

Table 3. Design domain for the two design optimization models.

Parameters	DOMP	DOM&KP
$R(\text{mm})$	$[70,100]$	$[70,100]$
AR	$[2.8,5.7]$	$[2.5,6]$
$f(\text{Hz})$	$[10,24]$	$[5,30]$
$\phi_m(°)$	90	$[0,90]$
$k_\eta(\text{Nm/rad})$	9.6×10^{-4}	$[1,15]\times10^{-4}$

% DOMP denotes design optimization for morphological parameters.
% DOM&KP denotes design optimization for morphological and kinematic parameters.

Table 4. Design optimization results for morphological parameters.

	$R(\text{mm})$	AR	$f(\text{Hz})$	$P^*(\text{W/kg})$	ε
Optimization results	96.9	3.32	18.7	23.83	42.9 %
Experimental results	90	4.63	18.0	41.73	---

$$\begin{cases} Find & X=[R \quad AR \quad f] \\ \min & f(X)=P^* \\ s.t. & 70\le R\le 100;\ 2.8\le AR\le 5.7 \\ & 10\le f\le 24;\ \ \dfrac{2Lift_{mean}}{mg}\ge 1. \end{cases} \tag{23}$$

where the kinematic parameters are provided as $[C_R \quad \phi_m \quad k_\eta]$ $=[25 \quad 90° \quad 9.6\times10^{-4}]$ according to the determination method in Secs. 3 and 4; P^* and $Lift_{mean}$ denote the total mass-normalized energy consumption and average lift during a flapping cycle, respectively; m stands for the weight of the prototype, and takes 17.2 g.

N = 500 is used for the subset simulation and gradient-based optimization is conducted with the initial point from the result of the subset simulation. The optimization results are shown in Table 4. From Table 4, we know that the energy consumption has decreased by 42.9 % compared with the experimental results.

The optimal geometric shape of the wing is provided in Fig. 8. Fig. 8 shows that the wing becomes greater far away from the flapping mechanism, which is contrary to the shape in the experiments. The time-varying Euler angles and produced lift force within two cycles are shown in Figs. 9 and 10, respectively. We see that the sweeping motion is approximately sinusoidal and the pitching angle also changes smoothly, which is greatly beneficial to the stable flapping flight. The lift force production is also a time-varying process during the flapping flight. From Fig. 10, we see that the produced lift force is less than 0 at some time duration. However, this does not affect the normal hovering of the MAV, as long as the average generated lift force can resist gravity.

The sensitivity of the lift force and energy consumption to each design parameters are provided in Fig. 11, which could verify why the results in Table 4 are globally optimal. Fig. 11 shows that the sensitivity of the lift force and energy consumption to each parameter is obviously different, and the sensitivity of the lift force and energy consumption to a given parameter is also different during the cycle. Take Fig. 11(a) for example, the sensitivity of energy consumption to R increases approximately before $R\le 80$, and then decreases when $R\in[80,96.9]$, and increases again after $R\ge 96.9$; while the sensitivity of the lift force to R increases during the whole cycle. The optimal R is the minimal energy consumption while the lift force is satisfied. As shown in Fig. 11(c),

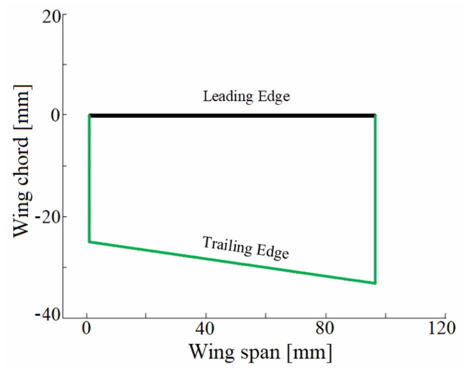

Fig. 8. Optimal shape after design optimization for morphological parameters.

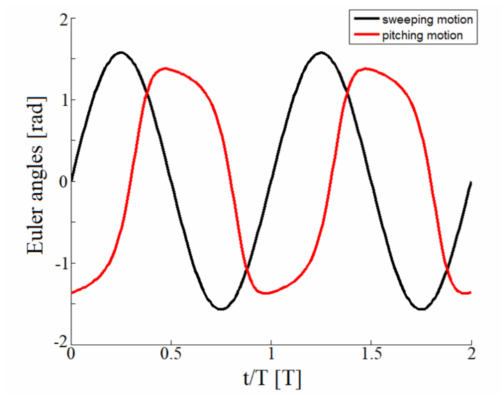

Fig. 9. Time-varying process of the sweeping and pitching motion in two cycles.

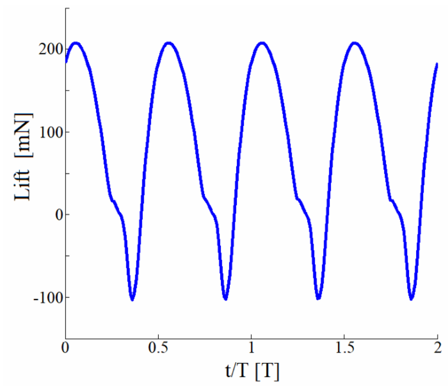

Fig. 10. Time-varying process of the lift force production in two cycles.

Table 5. Design optimization results for both morphological and kinematic parameters.

	$R(\text{mm})$	AR	$f(\text{Hz})$	ϕ_m	$k_\eta(\text{Nm/rad})$	$P^*(\text{W/kg})$	ε
Optimization results	100	4.14	18.7	88.9°	6.6×10^{-4}	22.70	45.6 %
Experimental results	90	4.65	18.0	90°	9.6×10^{-4}	41.73	---

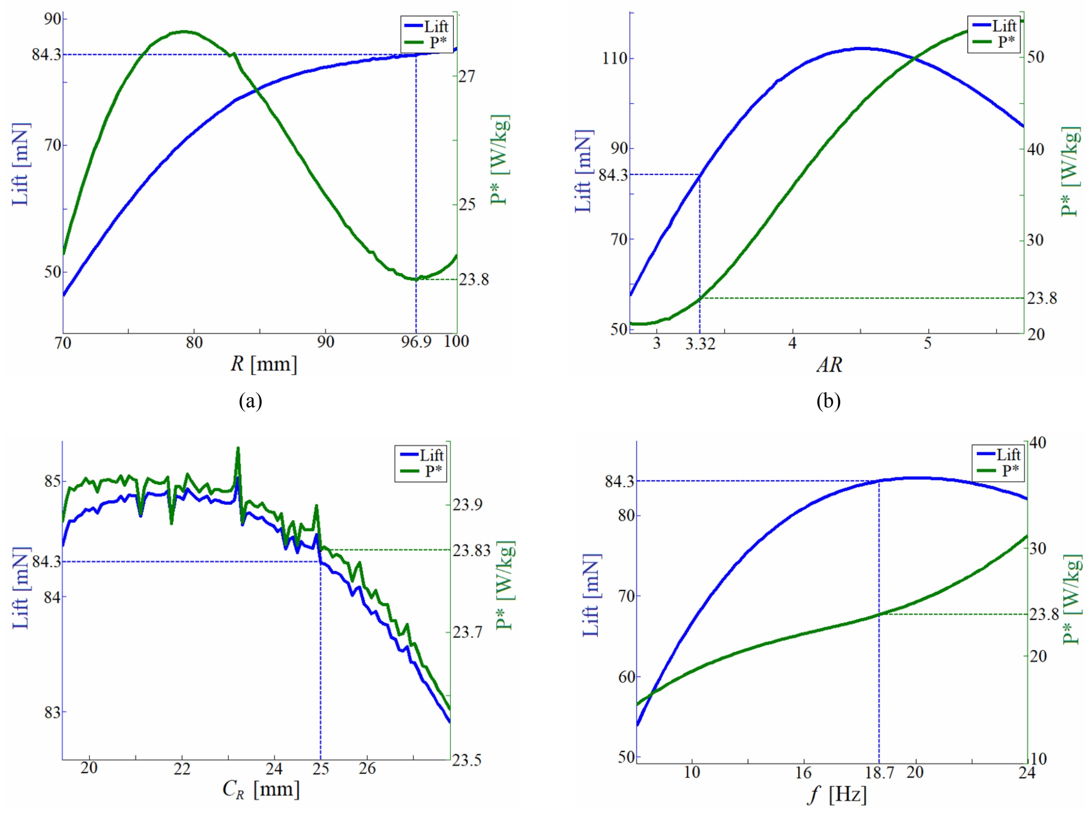

Fig. 11. Sensitivity of the lift force and energy consumption to each parameter.

numerical noise occurs when solving the ODE in Eq. (5), which is difficult to eliminate because of the existence of either truncation error or round-off error [8].

5.2 Design optimization for morphological and kinematic parameters

To further investigate the effects of the parameters of ϕ_m and k_η on the performance, e.g.: The lift force and power consumption, design optimization considering wing morphology and kinematics is carried out. The design optimization model is

$$\begin{cases} Find \quad X=\begin{bmatrix} R & AR & f & \phi_m & k_\eta \end{bmatrix} \\ \min \quad f(X)=P^* \\ s.t. \quad 70\le R\le 100;\quad 2.5\le AR\le 6; \\ \qquad 5\le f\le 30;\quad 1\times10^{-4}\le k_\eta\le 15\times10^{-4}; \\ \qquad 0\le \phi_m\le 90^\circ;\quad Lift_{mean}\ge 84.28. \end{cases} \tag{24}$$

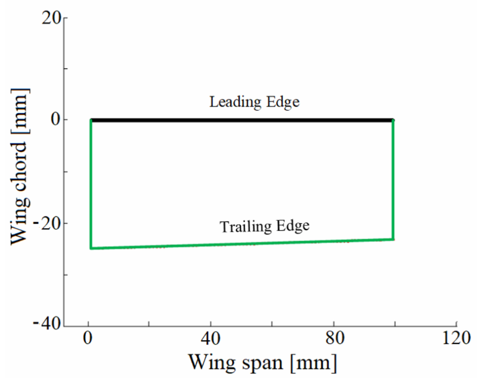

Fig. 12. Optimal shape after design optimization for morphological and kinematic parameters.

The combination of the subset simulation and gradient-based optimization method is also employed to solve the design optimization model, and the optimal results are shown in Table 5. Compared with the results in experiments, the energy consumption decreases by 45.6 % when the design optimiza-

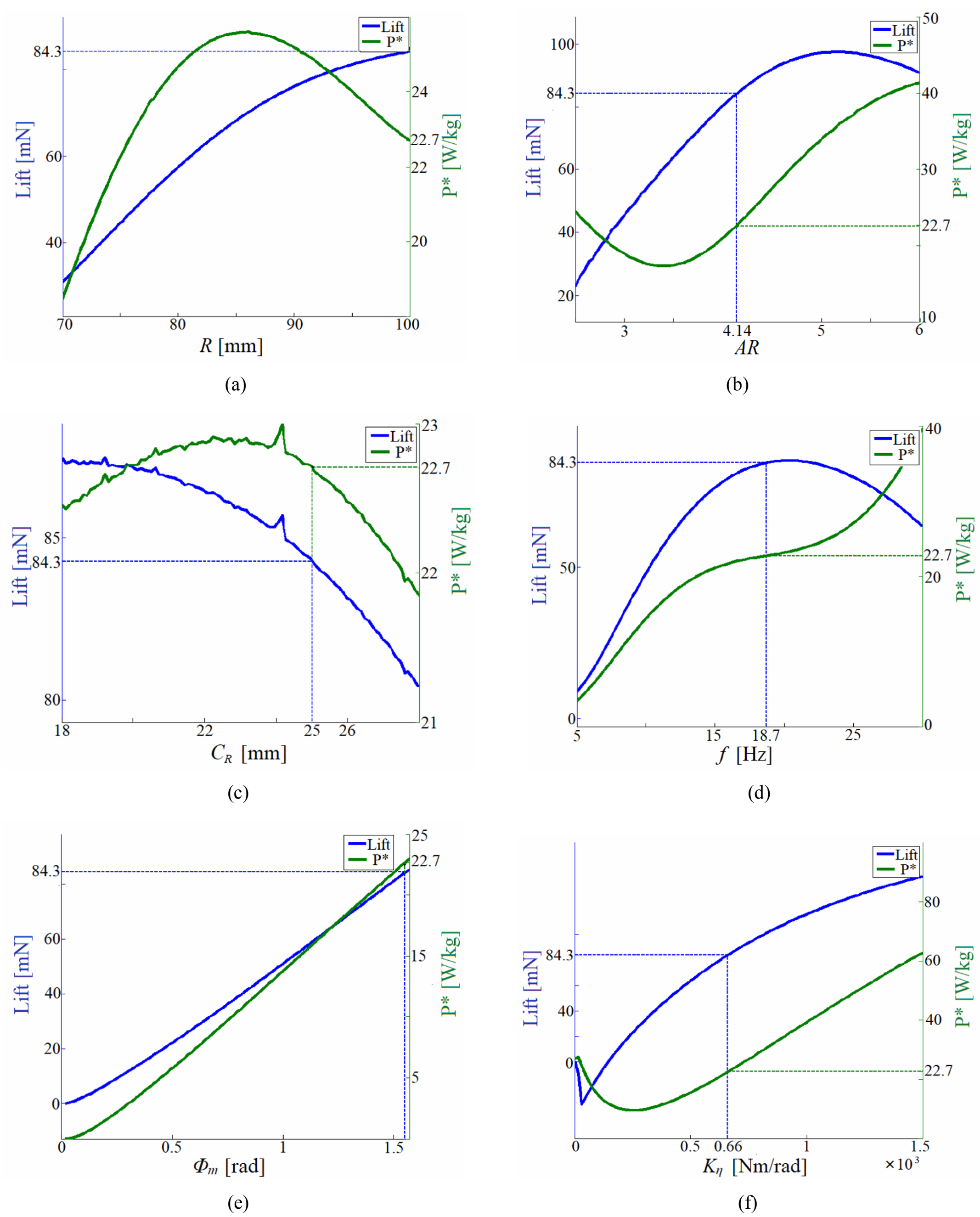

Fig. 13. Sensitivity of the lift force and energy consumption to each parameter.

tion is conducted by considering both morphological and kinematic parameters. Meanwhile, a conclusion is reached that the kinematic parameters still imposes effects on the lift force generation and energy consumption. Note that the optimization result of ϕ_m is very close to 90°, which is the optimal sweeping amplitude of many insects in the hovering flight, including fruitfly, bumblebee and hawkmoth [22].

The optimal shape of the wing by considering both morpho logical and kinematic parameters is shown in Fig. 12. From Fig. 12, we know that the shape is opposite by considering kinematic parameters additionally compared with only considering morphological parameters, which is consistent with the experimental shape. These two opposite results may be the embodiment of the low impact of C_R on lift force generation and energy consumption.

The influence of each parameter on the lift force generation and power consumption is shown in Fig. 13. The sensitivity curves are similar to those in Figs. 11(a)-(d) and 13(a)-(d). The sensitivity curves of the lift force and energy consumption to ϕ_m increase during the cycle. The sensitivity curves of the lift force and energy consumption to k_η rise first and then decrease during the cycle.

Table 6. Design optimization results for the location of pitching axis.

	$\hat{d}_r$	$\hat{d}_t$	k_η (Nm/rad)	f (Hz)	P^* (W/kg)	ε
Initial design results	0	0	9.6×10^{-4}	18.71	23.83	---
Optimal design results	0.33	0.08	2.0×10^{-4}	19.26	20.57	13.7 %

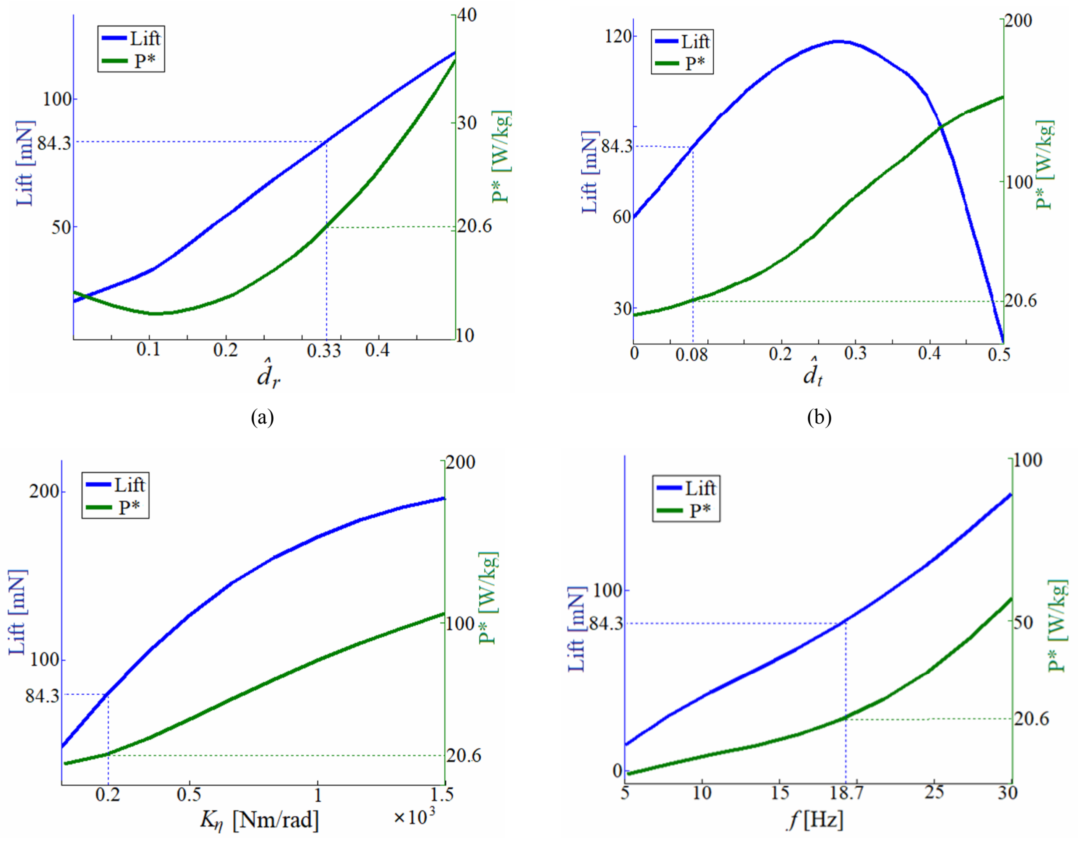

Fig. 14. Sensitivity of the lift force and energy consumption to each parameter.

5.3 Design optimization for the location of pitching axis

Although the wing shape, flapping kinematics and distributed wing stiffness have been investigated, the influence of the location of the wing pitching axis is not considered. However, the location of the pitching axis affects the lift force and power consumption. Therefore, it is selected as another design variable to study the effect in this part.

The normalized parameter $\hat{d}$ changes along the span, and the linear model is employed [27],

$$\hat{d}(x_c)=\frac{1}{R}\left(\hat{d}_t-\hat{d}_r\right)x_c+\hat{d}_r \tag{25}$$

where $\hat{d}_r$ and $\hat{d}_t$ are the values of the normalized parameter $\hat{d}$ at the wing root and wing tip, respectively, and $0\le\hat{d}(x_c)\le0.5$.

When the wing pitching axis changes, the distributed stiffness changes and therefore is considered as a design variable. Under the consideration of the effect of flapping frequency on the lift force and power consumption, the flapping frequency is also considered as the design variable. The design optimization model is constructed by

$$\begin{cases} Find \quad X=\left[\hat{d}_r \quad \hat{d}_t \quad k_\eta \quad f\right] \\ \min \quad f(X)=P^* \\ s.t. \quad 0\le\hat{d}_r\le0.5;\ \ 0\le\hat{d}_t\le0.5; \\ \qquad 1\times10^{-4}\le k_\eta\le15\times10^{-4}; \\ \qquad 5\le f\le30;\ \ \dfrac{2Lift_{mean}}{mg}\ge1. \end{cases} \tag{26}$$

The optimal design results and the initial design variables are provided in Table 6. It can be seen that the optimal pitching axis is not $\hat{d}=0$ but $\left[\hat{d}_r \quad \hat{d}_t\right]=\left[0.33 \quad 0.08\right]$. Compared to the initial condition $\hat{d}=0$, more wing area is put in the front of the pitching axis after optimization. Furthermore, 13.7 % energy will be saved since extra kinetic energy can be saved.

The sensitivity curves about the lift force and power consumption to each design parameters are provided in Fig. 14. It is clearly seen that $\hat{d}_r$, k_η and f are positively correlated with the lift force and energy consumption within the constraints. But for $\hat{d}_t$, the sensitivity curves of the lift force rises first and then decreases during the cycle.

6. Conclusions

We first employed DOE to select sensitive parameters for optimally designing the wing of a hummingbird-like MAV to decrease the computational expense during the design optimization procedure. As an important kinematic parameter, the distributed wing stiffness, was approximately estimated based on experimental data with the least square method, which provides the deterministic parameter for the design optimization to obtain the morphological parameters. Three design optimization models were then built by considering the morphological parameters, both morphological and kinematic parameters and the location of pitching axis, respectively. The combination of subset simulation and gradient-based optimization was finally presented to solve the three design optimization models and corresponding sensitivity analysis was conducted. With the design optimization, the energy consumption decreased by 42.9 %, 45.6 % and 13.7 % under the satisfaction of the produced lift force.

Acknowledgments

This work was supported by the National Natural Science Foundation of China under the Contract No. 11472075. The authors declare that they have no conflict of interest.

Nomenclature

R : Wing span
C_R : Wing root chord
C_T : Wing tip chord
AR : Aspect ratio
$\bar{c}$: Mean chord length
S : Wing area
$\hat{d}$: The chord-normalized distance from the pitching axis to the leading edge
ϕ_m : Sweeping amplitude
ϕ_0 : Horizontal offset
f : Frequency
θ_m : Heaving amplitude
Φ_θ : Heaving phase offset
θ_0 : Heaving offset
k_η : The distributed wing stiffness
$\boldsymbol{\omega}_c$: Angular velocity
$\boldsymbol{\alpha}_c$: Angular acceleration
ρ_f : Fluid density
$C_{F_{Y_c}}^{trans}$: Translational force coefficient
$\hat{z}_{cp}^{trans}$: Normalized chordwise center of pressure
$\hat{\alpha}$: Angle of attack
C_D^{rot} : Rotational damping coefficient
$\boldsymbol{\tau}^{iner}$: Inertial torque
P^* : Total mass-normalized power consumption
$\hat{d}_r$: $\hat{d}$ at the wing root
$\hat{d}_t$: $\hat{d}$ at the wing tip

References

[1] J. M. V. Rayner, A vortex theory of animal flight, Part 1. The vortex wake of a hovering animal, *J. of Fluid Mechanics Digital Archive*, 91 (4) (1979) 731-763.

[2] C. P. Ellington, The aerodynamics of hovering insect flight, I. The quasi-steady analysis, *Philosophical Transactions of the Royal Society B: Biological Sciences*, 305 (1122) (1984) 1-15.

[3] C. P. Ellington, The aerodynamics of hovering insect flight, II. Morphological parameters, *Philosophical Transactions of the Royal Society B: Biologi-cal Sciences*, 305 (1122) (1984) 17-40.

[4] C. P. Ellington, The aerodynamics of hovering insect flight, VI. Lift and power requirements, *Philosophical Transactions of the Royal Society B: Biological Sciences*, 305 (1122) (1984) 145-181.

[5] Q. Wang, J. F. L. Goosen and F. van Keulen, A predictive quasi-steady model of aerodynamic loads on flapping wings, *J. of Fluid Mechanics,* 800 (2016) 688-719.

[6] Q. Wang, J. F. L. Goosen and F. van Keulen, Study of design parameters of flapping-wings, *IMAV 2013: International Micro Air Vehicle Conference and Competition*, Delft, Netherlands (2014).

[7] Q. Wang, J. F. L. Goosen and F. van Keulen, Optimal pitching axis of flapping-wings for hovering flight, *Engineering Optimization*, Lisbon, Portugal (2014).

[8] Q. Wang, J. F. L. Goosen and F. van Keulen, Optimal hovering kinematics with respect to various flapping-wing shapes, *IMAV 2013: Proceedings of the International Micro Air Vehicle Conference and Flight Competition*, Toulouse, France (2013).

[9] H. J. Peters, The optimization of the flapping wings for a micro air vehicle, *Master Thesis*, Delft University of Technology (2011).

[10] H. J. Peters, J. F. L. Goosen and F. V. Keulen, Optimal FWMAV wing design for a combination of energy-effective hovering and roll control, *International J. of Micro Air Vehicles*, 7 (1) (2015) 41-53.

[11] Y. Nan, M. Karasek, M. Lalami and H. Altartouri, An experimental study on effect of wing geometry of hummingbird-like flapping wing in the hover, *International Micro Air Vehicles Conference and Flight Competition*, Aachen, Germany (2015).

[12] S. P. Sane, The aerodynamics of insect flight, *J. of Experimental Biology*, 206 (23) (2003) 4191-4208.
[13] E. C. Stewart, M. J. Patil, R. A. Canfield and R. D. Snyder, Parametric representation and shape optimization of flapping micro air vehicle wings, *International J. of Micro Air Vehicles*, 4 (4) (2012) 179-202.
[14] M. Ghommem, N. Collier, A. H. Niemi and V. M. Calo, On the shape optimization of flapping wings and their performance analysis, *Aerospace Science and Technology*, 32 (1) (2014) 274-292.
[15] D. R. Warrick, B. W. Tobalske and D. R. Powers, Aerodynamics of the hovering hummingbird, *Nature*, 435 (7045) (2005) 1094-1097.
[16] M. Keennon, K. Klingebiel, H. Won and A. Andriukov, Development of the nano hummingbird: A tailless flapping wing micro air vehicle, *Aiaa Aerospace Sciences Meeting Including the New Horizons Forum & Aerospace Exposition*, Tennessee, USA (2012).
[17] M. Karásek, Y. Nan, I. Romanescu and A. Preumont, Pitch moment generation and measurement in a robotic hummingbird, *International J. of Micro Air Vehicles*, 5 (4) (2013) 299-309.
[18] S. Mao and D. Gang, Lift and power requirements of hovering insect flight, *J. of Mechanics*, 19 (5) (2003) 458-469.
[19] M. H. Dickinson and J. R. B. Lighton, Muscle efficiency and elastic storage in the flight motor of Drosophila, *Science*, 268 (5207) (1995) 87-90.
[20] R. Dudley, *The Biomechanics of Insect Flight: Form, Function, Evolution*, Princeton University Press, Princeton, USA (2000).
[21] J. M. Wakeling and C. P. Ellington, Dragonfly flight, III. Lift and power requirements, *J. of Experimental Biology*, 200 (3) (1997) 583-601.
[22] G. J. Berman and Z. J. Wang, Energy-minimizing kinematics in hovering insect flight, *J. of Fluid Mechanics*, 582 (2007) 153-168.
[23] M. I. Woods, J. F. Henderson and G. D. Lock, Energy requirements for the flight of micro air vehicles, *The Aeronautical J.*, 105 (1045) (2001) 135-149.
[24] R. Madangopal, Z. A. Khan and S. K. Agrawal, Energetics-based design of small flapping-wing air vehicles, *IEEE/ASME Transactions on Mechatronics*, 11 (4) (2006) 433-438.
[25] A. L. Schwab and J. P. Meijaard, How to draw Euler angles and utilize Euler parameters, *International Design Engineering Technical Conferences and Computers and Information in Engineering Conference*, Philadelphia, USA (2006) 259-265.
[26] M. F. M. Osborne, Aerodynamic of flapping flight with application to insects, *J. of Experimental Biology*, 28 (2) (1951) 221-245.
[27] Q. Wang, J. F. L. Goosen and F. van Keulen, Optimal pitching axis location of flapping wings for efficient hovering flight, *Bioinspiration & Biomimetics,* 12 (5) (2017) 056001.
[28] Z. Wang, X. Cheng and J. Liu, Time-dependent concurrent reliability-based design optimization integrating experiment-based model validation, *Structural and Multidisciplinary Optimization*, 57 (4) (2018) 1523-1531.
[29] S. Yu, Z. Wang and K. Zhang, Sequential time-dependent reliability analysis for the lower extremity exoskeleton under uncertainty, *Reliability Engineering & System Safety*, 170 (2018) 45-52.
[30] Z. Wang, Z. P. Mourelatos, J. Li, I. Baseski and A. Singh, Time-dependent reliability of dynamic systems using subset simulation with splitting over a series of correlated time intervals, *J. of Mechanical Design*, 136 (6) (2014) 1-12.
[31] Z. Wang, X. Zhang, H. Huang and Z. P. Mourelatos, A simulation method to estimate two types of time-varying failure rate of dynamic systems, *J. of Mechanical Design*, 138 (12) (2016) 1-10.
[32] H. S. Li and S. K. Au, Design optimization using subset simulation algorithm, *Structural Safety*, 32 (6) (2010) 384-392.

Zhonglai Wang is a Professor of Mechanical Engineering at University of Electronic Science and Technology of China where he received his Ph.D. in 2009. His research interests include design optimization of flapping wing micro aerial vehicles (FWMAVs), system reliability modeling, reliability-based design optimization, robust design and model validation.

Xiaorong Hu obtained his M.S. in Mechatronics Engineering at University of Electronic Science and Technology of China. His research interests include performance analysis and design optimization of flapping wing micro aerial vehicles s (FWMAVs).

Yingdong Wu is a Master's student in Mechatronics Engineering at University of Electronic Science and Technology of China. His research interests include design optimization of flapping wing micro aerial vehicles (FWMAVs).